12-8-2010

Flow Vision for Autonomous Underwater Vehicles via an Artificial Lateral Line

Nam Nguyen

Douglas L. Jones

Yingchen Yang

Chang Liu

Hindawi Publishing Corporation
EURASIP Journal on Advances in Signal Processing
Volume 2011, Article ID 806406, 11 pages
doi:10.1155/2011/806406

Research Article

Flow Vision for Autonomous Underwater Vehicles via an Artificial Lateral Line

Nam Nguyen,[1] Douglas L. Jones,[1] Yingchen Yang,[2] and Chang Liu[3]

[1] *Department of Electrical and Computer Engineering, University of Illinois at Urbana Champaign, 1308 West Main Street, Urbana, IL 61801, USA*
[2] *Department of Engineering, University of Texas at Brownsville, 80 Fort Brown, Brownsville, TX 78520, USA*
[3] *Department of Mechanical Engineering, Northwestern University, 2145 Sheridan Road, Evanston, IL 60208, USA*

Correspondence should be addressed to Nam Nguyen, nnguyen5@illinois.edu

Received 15 June 2010; Accepted 23 November 2010

Academic Editor: Raviraj S. Adve

Most fish have the capability of sensing flows and nearby movements even in dark or murky conditions by using the lateral line organs. This enables them to perform a variety of underwater activities, such as localizing prey, avoiding predators, navigating in narrow spaces, and schooling. To emulate this capability for Autonomous Underwater Vehicles, we developed an artificial lateral line using an array of Micro-Electro-Mechanical-Systems (MEMS) flow sensors. The signals collected via the artificial lateral line are then processed by an adaptive beamforming algorithm developed from Capon's method. The system produces 3D images of source locations for different hydrodynamic activities, including the vibration of a dipole source and the movement of a tail-flicking crayfish. A self-calibration algorithm provides the capability of self-adaptation to different environments. Lastly, we give a Cramer-Rao bound on the theoretical performance limit which is consistent with experimental results.

1. Introduction

Most fish can sense dynamic flows using the lateral-line sensory organs along their bodies [1] (Figure 1(a)). A lateral line consists of numerous tiny hair-cell receptors, which invoke neural spiking when moving fluid causes the hairs to bend (Figures 1(b) and 1(c)). Fish use this sensing capability to perform a wide range of activities including navigating in dark and murky water, localizing prey, avoiding predators, and schooling [2–5].

Thanks to recent developments in Micro-Electro-Mechanical-Systems (MEMS) technology, it is now possible to realize this sensing capability on Autonomous Underwaters Vehicles with artificial hair-cell sensors [6]. The MEMS sensor also has a micrometer-scale hair which bends when intercepting a flow. Depending on the level of bending, the mechanical force applied to the hair is translated to an electrical signal with a certain magnitude. Those sensors can be mass-produced and cheaply assembled into a larger sensing system like a man-made lateral line [7].

An artificial lateral line itself is not a complete functional system without a signal processing unit. One primary goal of the signal-processing unit is to localize or map the surrounding dynamic flow activities. Curcic-Blake and van Netten applied a continuous wavelet transform on the excitation signals collected directly from a real ruffle fish (*Gymnocephalus cernuus L.*) [8]. A 2D-contour map of the area surrounding a dipole source is generated but with very low resolution. In this paper, we provide a new approach using a beamforming technique (i.e., Capon's method) to achieve a much sharper 3D-image of the dipole sources.

Calibration is an important process for a real sensory system to compensate sensors' discrepancies and then to enhance the system's performance. A self-calibration algorithm is introduced to tune the sensors online during operation.

Finally, we also derive the theoretical performance limit, which can help to understand fundamental limitations of lateral-line systems and to provide guidance in their design and use.

This paper completes the series of our work on artificial lateral line which has been reported in [9–11].

2. Artificial Lateral-Line

Figure 1(e) illustrates a man-made hair-cell sensor consisting of a horizontal cantilever with a vertical hair attached at the distal end and an embedded piezoresistor at the fixed end. When a flow impinges upon the vertical hair, a bending force acts on the horizontal cantilever to induce a stress change at the piezoresistor, causing a change in resistance (Figure 1(f)). When an electric current runs through the piezoresistor, the change in the resistance will cause a change in the voltage across the sensor. Within an operational range, the change in electrical signal strength is linearly proportional to the change in the force acting on the hair, which can be used to infer the local flow velocity [7, 12, 13].

Note that, due to its physical structure, the sensor is sensitive to flows along the direction of the horizontal cantilever and almost insensitive to flows in the perpendicular direction. By inspecting a number of sample sensors, we find that the sensor's directivity pattern or response function is approximately a figure-eight shape with two peaks (top and bottom of the figure-eight shape) lying along the direction of the horizontal cantilever. Therefore, the direction of the horizontal cantilever defines the orientation of the sensor, an important parameter when assembling sensors into an artificial lateral line.

Using these MEMS sensors, an artificial lateral line can be built and installed on AUVs for sensing surrounding flow activities. Figure 1(d) shows the working prototype of a lateral line consisting of 15 sensors on a half-cylinder surface which models the body of an AUV. The cylinder has an outer diameter of 89 mm and a length of 240 mm. There are 9 sensors along the central line of the cylinder surface with linear spacing of 30 mm, and 6 sensors on both sides of the middle cross curvature with angular spacing of 30°. Also note the alternating pattern of sensors' orientation. This configuration is selected to achieve a good 3D localization performance with a limited number of sensors based on numerical evaluation of the Cramer-Rao lower bound.

One of the most common forms of water disturbance that is extensively used as a stimulus to study fish lateral-line organs is the acoustic dipole source or a sinusoidally vibrating sphere [15]. Since dipole motions are also the main components in the model of fish's tail-beating movement, these responses can also be used to localize many real-world sources such as a tail-flicking crayfish.

2.1. Model of Sensor Response to a Dipole Source. Consider a dipole source of diameter a placed at the origin and oscillating along the z-axis at frequency f and amplitude U_o, that is, $z(t) = U_o \sin(2\pi f t)$. The flow velocity at all points at distance r and symmetrically positioned around the z-axis by angle θ is derived in [16] as

$$\vec{v}_{\text{flow}}(r,\theta) = \left(a^3 U_o \frac{\cos(\theta)}{r^3}\right)\hat{\mathbf{r}} + \left(\frac{a^3 U_o}{2}\frac{\sin(\theta)}{r^3}\right)\hat{\boldsymbol{\Theta}}, \quad (1)$$

where $\hat{\mathbf{r}}$ and $\hat{\boldsymbol{\Theta}}$ are unit vectors of the dipole's spherical coordinates at the sensor's position as shown in Figure 2(a). Equation (1) indicates the flow velocity at any sensor location around the dipole source. Since we are more interested in knowing the sensor's response relative to the dipole location with respect to the sensor, it is more convenient to translate (1) from the dipole's spherical coordinates to the lateral line's Cartesian coordinates as shown in Figure 2(b). So if in the lateral-line's Cartesian coordinates, $\vec{s} = (x_s, y_s, z_s)$ specifies the position of a sensor and $\vec{d} = (x_d, y_d, z_d)$ indicates the location of the dipole source, then the flow velocity seen at the sensor is

$$\vec{v}_{\text{flow}}\left(\vec{d}\right) = \frac{a^3 U_o}{2r^3}(3\cos(\theta)\hat{\mathbf{r}} - \hat{\mathbf{z}}_d), \quad (2)$$

where $\hat{\mathbf{z}}_d$ is the unit vector specifying the oscillating direction of the dipole source, and

$$r = \left\|\vec{s} - \vec{d}\right\|, \quad \hat{\mathbf{r}} = \frac{\vec{s} - \vec{d}}{\left\|\vec{s} - \vec{d}\right\|}. \quad (3)$$

From (2), it is clear that the flow velocity impacting on the sensor's hair is not necessarily in the horizontal plane of the cantilever. In that case, we can project the flow velocity $\vec{v}_{\text{flow}}$ onto the horizontal plane and approximate that projected component $\vec{v}_{\perp}$ as the final flow velocity sensed by the sensor's hair. Therefore, the vector that defines the horizontal plane (which also defines the direction of the sensor's hair) is also an important parameter of the sensor. So a sensor in a lateral line is determined by three vectors: the position vector $\vec{s}$, the orientation vector $\vec{u}$, and the hair direction vector $\vec{h}$ as shown in Figure 1(e).

Also recall that the directivity pattern or the response function of a sensor has a figure-8 shape. So if α is the angle between the orientation vector $\vec{u}$ and $\vec{v}_{\text{flow}}^{\perp}$ is the projection of the flow velocity onto the horizontal plane, we can model the sensor response of the dipole source at location $\vec{d}$ as

$$f\left(\vec{d}\right) = \left\|\vec{v}_{\text{flow}}^{\perp}\right\|(a\cos\alpha + b\sin\alpha + c), \quad (4)$$

where a, b, c are the directivity parameters defining the figure-8-shaped response pattern. For an ideal sensor, we should have $a = 1$, $b = c = 0$. In practice, those parameters will be computed for each sensor by a self-calibration algorithm explained later.

3. Flow-Imaging Algorithm

With the artificial lateral line as the hardware platform to collect signals from the outside world, we need to develop a signal-processing algorithm to process those collected signals. The goal of the signal-processing algorithm is to produce a 3D image of the energy-level distribution of flow-creating moving objects in the surroundings. The approach is to scan all possible source locations in the

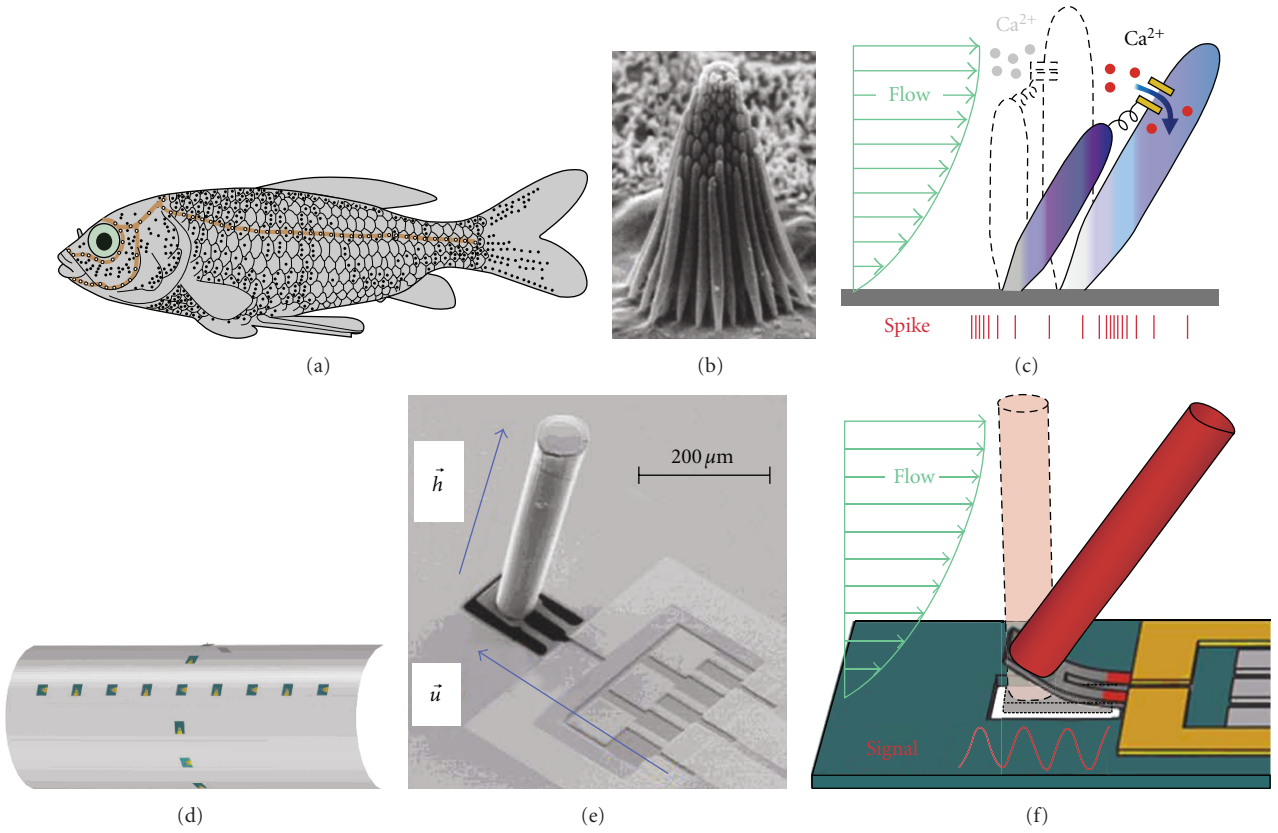

FIGURE 1: (a) Distribution of neuromasts, a cluster of hair-cell organs indicated by black dots, on a *Carassius auratus* goldfish's body (modified from Schmitz et al. [14]). (b) A close-up image of a neuromast which is made of many hairs. (c) Illustration of a neuromast's function to generate excitation spikes when hairs are bended. (d) Testing platform with 15 artificial hair-cell sensors. (e) A close-up image of a sensor. (f) Operation principle of the artificial hair-cell sensor. All (c)–(f) are modified from [11].

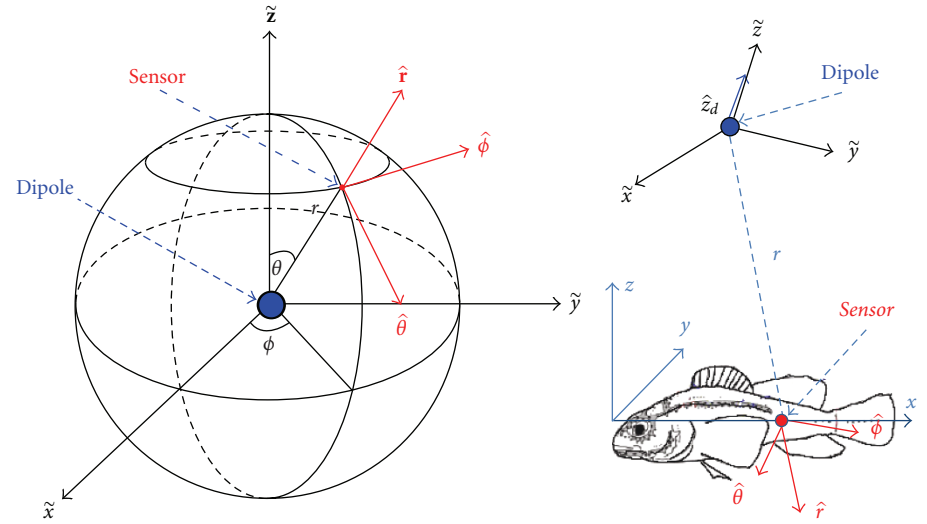

FIGURE 2: Translating the flow velocity vector at a sensor location impact by a dipole in different coordinate systems. (a) The flow velocity in the dipole's spherical coordinates with (r, θ, ϕ) defining the location of a sensor with repect to the dipole and $(\hat{\mathbf{r}}, \hat{\theta}, \hat{\phi})$ defining the unit vectors of the dipole's spherical coordinates at the sensor's position (modified from [16]). (b) Flow velocity is computed in the lateral line's Cartesian coordinates (modified from [10]).

surrounding region and to compute an estimate of the level of agreement between the measured excitation array pattern and the expected pattern assuming a dipole source at that location. The expected patterns can be derived from the analytical model in (2) and (4) or from training templates. Different algorithms may produce different estimates. In [8], the authors used a continuous wavelet transform (CWT) technique to produce a 2D-contour map. From such a map, we can infer the region of a single dipole source, but the CWT has very low resolution so the source is difficult to locate precisely, and multiple sources probably could not be distinguished. Similarly, in [17] we used a mean squared-error function to generate 2D images for detection and localization of a single source. Although this method is a maximum likelihood estimator under single-source assumptions, it also produces low-resolution images.

Our approarch here is based on a minimum-variance beamforming framework, or Capon's method. In particular, assume that there are N sensors in the array and we sample K possible source locations surrounding the array (i.e., $\vec{d}_k$ with $1 \le k \le K$). Let $\mathbf{c}$ be a vector of the measured data from the array and $\mathbf{e}_k$ be the expected array pattern stimulated by a dipole source at position $\vec{d}_k$; that means $\mathbf{e}_k = [f_1(\vec{d}_k), f_2(\vec{d}_k), \ldots, f_N(\vec{d}_k)]^T$ where $f_n(\vec{d}_k)$ is the response of sensor n according to the model in (2) and (4). The basic concept of the minimum-variance beamforming framework is that for each scanned location k, an optimal weight vector $\mathbf{w}_k$ is applied to the sensor data to recover the signal from the point k while maximally suppressing the noise and signals from other locations. Mathematically, $\mathbf{w}_k$ is the solution to the optimization problem

$$\min_{\mathbf{w}_k} E\left[\left|\mathbf{w}_k^H \mathbf{c}\right|^2\right] \text{ subject to } \Re\left[\mathbf{w}_k^H \mathbf{e}_k\right] = 1 \tag{5}$$

which is given by [18] as

$$\mathbf{w}_k = \frac{\mathbf{R}^{-1}\mathbf{e}_k}{\mathbf{e}_k^H \mathbf{R}^{-1}\mathbf{e}_k} \tag{6}$$

and the final output power corresponding to location k is

$$\frac{1}{\mathbf{e}_k^H \mathbf{R}^{-1}\mathbf{e}_k}, \tag{7}$$

where $\mathbf{R}$ is the correlation matrix of the sensor array signals [18] and $\mathbf{w}_k^H, \mathbf{e}_k^H$ are Hermitian transposes of $\mathbf{w}_k, \mathbf{e}_k$, respectively.

Applying Capon's method, we can build the flow imaging algorithm as follows.

Step 1. Using the analytical model from (2) and (4), compute the expected array pattern $\mathbf{e}_k$ for all locations of interest $1 \le k \le K$

$$\mathbf{e}_k = \left[f_1\left(\vec{d}_k\right), f_2\left(\vec{d}_k\right), \ldots, f_N\left(\vec{d}_k\right)\right]^T. \tag{8}$$

Note that the sensor response depends not only on the position vector $\vec{d}_k$ but also on the oscillation orientation of the dipole source which is defined by the azimuth angle θ_d and the zenith angle ϕ_d. Therefore, there are actually two more angular dimensions to scan through for each point k.

Step 2. Compute the pseudocorrelation matrix or the outer-product of the signals measured from all sensors. If the signals from all sensors are sampled for a certain duration to collect L samples for each channel, that is, $\mathbf{c}[i]$ for $i = (1, 2, \ldots, L)$, then the outer-product-based empirical estimate of the correlation matrix is

$$\mathbf{R} = \frac{1}{L}\sum_{i=1}^{L} \mathbf{c}^H[i] * \mathbf{c}[i]. \tag{9}$$

Step 3. Use Capon's method to compute the energetic magnitude of any flow source at each scanned location k

$$E_k = \frac{1}{\mathbf{e}_k^H \mathbf{R}^{-1}\mathbf{e}_k}. \tag{10}$$

Step 4. Plot the energy-level 3D image with E_k representing the energy at point k in the space. The high-energy regions in the image correspond to the locations of dipole sources.

This algorithm implementing Capon's method produces much higher resolution 3D images of flow activities than the other two algorithms mentioned above.

4. Self-Calibration Algorithm

Calibration is an indispensable step when working with actual physical systems. The performance of a system can be significantly enhanced if the system is calibrated well; in many cases, accurate calibration is essential even to get intelligible results. In our case, each of these MEMS flow sensors in the array has different gain sensitivity and directivity pattern due to manufacturing and installation. This is especially true with sensors that are still in the laboratory stage of development. Even with commercial sensors operating long-term in an open environment such as an array deployed on an AUV, online calibration to compensate for environmental drift or damage is essential to maintain good performance. Calibration is therefore an essential preprocessing step to enhance performance and to support practical deployment of the system.

In Section 2.1, the total response of a sensor is modeled as $(a\cos\alpha + b\sin\alpha + c)$, which can be rewritten as $g(\cos\alpha + \lambda\sin\alpha + \mu)$ where $g = a, \lambda = b/a,$ and $\mu = c/a$. Hence, the two parameters λ and μ are directivity coefficients defining the shape and orientation of a figure-8 directivity pattern, while the parameter g is the total gain which captures both the mechanical and electrical gains of the whole sensor channel from the mechanical bending of the hair to the output of the final electrical signal amplifier or analog-to-digital converter.

The calibration process can be separated into the sensor directivity-pattern calibration and the sensor gain calibration. The sensor-directivity pattern calibration determines the two directivity parameters λ and μ. It can be done easily before installation on the array platform by measuring the signal strength of the sensor under test when moving a dipole

source circularly around the sensor at a fixed distance. If there are n testing points on the circle, for each point i we have sensor reading $y_i = (a\cos\alpha_i + b\sin\alpha_i + c)$ with the known angle α_i. We can then formulate the problem as a system of linear equations:

$$\begin{bmatrix} y_1 \\ y_2 \\ \vdots \\ y_n \end{bmatrix} \approx \begin{bmatrix} \cos\alpha_1 & \sin\alpha_1 & 1 \\ \cos\alpha_2 & \sin\alpha_2 & 1 \\ \vdots & \vdots & \vdots \\ \cos\alpha_n & \sin\alpha_n & 1 \end{bmatrix} \begin{bmatrix} a \\ b \\ c \end{bmatrix} \tag{11}$$

or

$$\mathbf{y} \approx \mathbf{A}\begin{bmatrix} a & b & c \end{bmatrix}^T. \tag{12}$$

So a, b, c in (12) can be solved as $[a \;\; b \;\; c]^T = (\mathbf{A}^T\mathbf{A})^{-1}\mathbf{A}^T\mathbf{y}$ to best fit the sensor readings $\mathbf{y}$ in a least-squared error sense. Therefore, we can estimate the directivity parameters $\lambda = b/a$ and $\mu = c/a$, which are independent of the size of the testing circle. This calibration process can also be applied after the installation of sensors on the platform.

The sensor gain calibration involves computing the relative gains of all sensors on the platform. We jointly fit the gains of all sensors so as to minimize the squared error with respect to the expected model. Therefore, this process is also called the lateral-line calibration. Since each sensor may react differently to the change of surrounding conditions (e.g., temperature, density, biofouling, etc.), the relative gains may deviate gradually by time and place. In this paper, we provide an online self-calibration algorithm that can help the system update the gains during operation.

In the rest of this section, we explain the general concept of the self-calibration algorithm and refer readers to the next section for a specific deployment of this algorithm in our system. Suppose a dipole source moves along a known path such as a straight line during the calibration process (which would commonly occur with a moving vessel passing a stationary dipole or vice versa), measurements are taken for M positions spaced at equal distance along the path. Denoting $\vec{d}_0$ and $\vec{d}^*$ as the initial position and spacing vectors, then all M positions are $\vec{d}_0, \vec{d}_0 + \vec{d}^*, \ldots, \vec{d}_0 + (M-1)\vec{d}^*$. With N sensors attached to the platform, the expected response of sensor i from the dipole at position j can be computed using (2) and (4) as

$$g_i f_i\left(\vec{d}_0 + (j-1)\vec{d}^*\right). \tag{13}$$

Scanning through M dipole positions produces the measurement matrix $\mathbf{C}$ for M expected array patterns:

$$\mathbf{C} \approx \begin{bmatrix} g_1 f_1\left(\vec{d}_0\right) & g_2 f_2\left(\vec{d}_0\right) & \cdots & g_N f_N\left(\vec{d}_0\right) \\ g_1 f_1\left(\vec{d}_0 + \vec{d}^*\right) & g_2 f_2\left(\vec{d}_0 + \vec{d}^*\right) & \cdots & g_N f_N\left(\vec{d}_0 + \vec{d}^*\right) \\ \vdots & \ddots & \ddots & \vdots \\ g_1 f_1\left(\vec{d}_0 + (M-1)\vec{d}^*\right) & g_2 f_2\left(\vec{d}_0 + (M-1)\vec{d}^*\right) & \cdots & g_N f_N\left(\vec{d}_0 + (M-1)\vec{d}^*\right) \end{bmatrix}. \tag{14}$$

The aim of calibration is to find a set of sensor gains $[g_1, g_2, \ldots, g_N]$ and position parameters $\vec{d}_0, \vec{d}^*$ in order to approximate $\mathbf{C}$ as closely as possible. The position parameters $\vec{d}_0, \vec{d}^*$ can be used as indicators of the approximation accuracy.

In the model for the measurement matrix $\mathbf{C}$ above, the right-hand side can be separated into two matrices, one as a linear function of sensor gains $[g_1, g_2, \ldots, g_N]^T$ and the other as a nonlinear function of $\vec{d}_0, \vec{d}^*$:

$$\mathbf{C} \approx \begin{bmatrix} f_1\left(\vec{d}_0\right) & f_2\left(\vec{d}_0\right) & \cdots & f_N\left(\vec{d}_0\right) \\ f_1\left(\vec{d}_0 + \vec{d}^*\right) & f_2\left(\vec{d}_0 + \vec{d}^*\right) & \cdots & f_N\left(\vec{d}_0 + \vec{d}^*\right) \\ \vdots & \ddots & \ddots & \vdots \\ f_1\left(\vec{d}_0 + (M-1)\vec{d}^*\right) & f_2\left(\vec{d}_0 + (M-1)\vec{d}^*\right) & \cdots & f_N\left(\vec{d}_0 + (M-1)\vec{d}^*\right) \end{bmatrix} \begin{bmatrix} g_1 & 0 & \cdots & 0 \\ 0 & g_2 & \cdots & 0 \\ \vdots & \ddots & \ddots & \vdots \\ 0 & 0 & \cdots & g_N \end{bmatrix}. \tag{15}$$

The problem becomes a mixed linear-nonlinear least-squares problem, which can be solved via an iterative approach by alternately optimizing between nonlinear and linear coefficients while keeping the other fixed [19]. The algorithm is summarized as follows.

Step 1. Initialize with uniform gains $g_1 = g_2 = \cdots = g_N = 1$ and initial values for $\vec{d}_0, \vec{d}^*$.

Step 2. Fix the position vectors $\vec{d}_0, \vec{d}^*$, and compute the gains $g_1, g_2, \ldots, g_N$ as a least-squares solution to best fit the measurement matrix **C** in (15).

Step 3. Fix the gains, then use a gradient method to search for next values of the nonlinear parameters $\vec{d}_0, \vec{d}^*$ that minimize the Frobenius norm between the measurement matrix **C** and the optimized product on the right-hand side of (15).

Step 4. Iterate Steps 2 and 3 until the Frobenius norm is small enough or $\vec{d}_0, \vec{d}^*$ converge asymptotically to some values. Usually the number of iterations can be set manually after some trials.

Note that the algorithm can be applied for any number of nonlinear parameters as long as the number of measurements exceed that of the unknowns. To simplify the explanation, we just use two position parameters $\vec{d}_0, \vec{d}^*$ to specify M locations of the dipole source (i.e., a straight-line path) for calibration. However, we actually use four position parameters (two along the axis and two along the arc of the cylinder) to define locations of the calibrated source in our experiment.

5. Experiments

So far, we have presented all main components of our lateral-line system from sensor hardware, analytical sensor response models, to self-calibration and signal processing algorithms. To show how those components work together in practice, we present the results of a complete experimental procedure from setting up the system, calibrating sensors and the lateral line, to generating the final outputs.

5.1. Experiment Setup. Figure 3 displays the setup of the experiment. A dipole source powered by an electric motor and moving up and down at a frequency of 45 Hz with a peak-to-peak amplitude of 10 mm is fixed at the center of a large water tank. A cylinder is used to attach 15 sensors in a cross formation as described in Section 2. The cylinder is attached on a metal frame to allow easy adjustment of its position and angle relative to the dipole source. Denoting the effective length of the cylinder (the largest distance between any two sensors) as one body length unit (BL = 240 mm), we mainly work with the dipole source within the near-field range of 0.5BL to the surface of the cylinder. Beyond this distance, the signal strength and localization resolution fall off rapidly. The dipole orientation and offset position

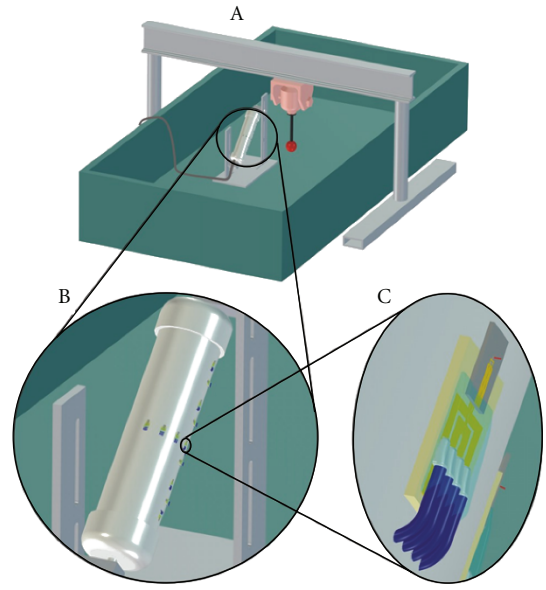

Figure 3: Experiment setup with the sensor arrays installed on a cylinder. A shaking machine controls the vibration of an dipole. The cylinder can be slid on a vertical frame to change relative vibration direction of the dipole to the sensors.

(position projected on the cylinder surface) can be changed by adjusting the cylinder frame position and sliding the cylinder on the frame.

5.2. Calibration. In order to achieve best performance, both the individual sensors and the overall lateral line need to be calibrated. Sensor calibration aims at computing the directivity parameters defining the figure-8-shaped directivity pattern. Ideally, this can be done after the manufacturing process by measuring the sensor response with a dipole source circling around it at a fixed range. In our experiment, we ran a number of tests with different dipole positions and used the Minimum Mean Square Estimator (MMSE) to best fit our model to the collected data.

The calibration of the lateral line (the sensor gain estimation) applies the self-calibration algorithm explained in Section 4. Specifically, we collect calibration data by stepping the dipole source from one sensor to the next one at 0.5 BL range. For each run, we compute the array pattern by extracting the signal strength at the dipole frequency (45 Hz). Note that the testing dipole source actually moves along the central line and then along the cross-curvature line at the middle. Therefore, we have two initial position vectors and two step-sizes (longitudinal and angular) as the nonlinear parameters to be estimated in the self-calibration algorithm.

5.3. Dipole Imaging. Before we can apply the beamforming algorithm to localize a dipole source at arbitrary positions and vibrating directions, we need to compute the expected array patterns for the dipole source at all the locations

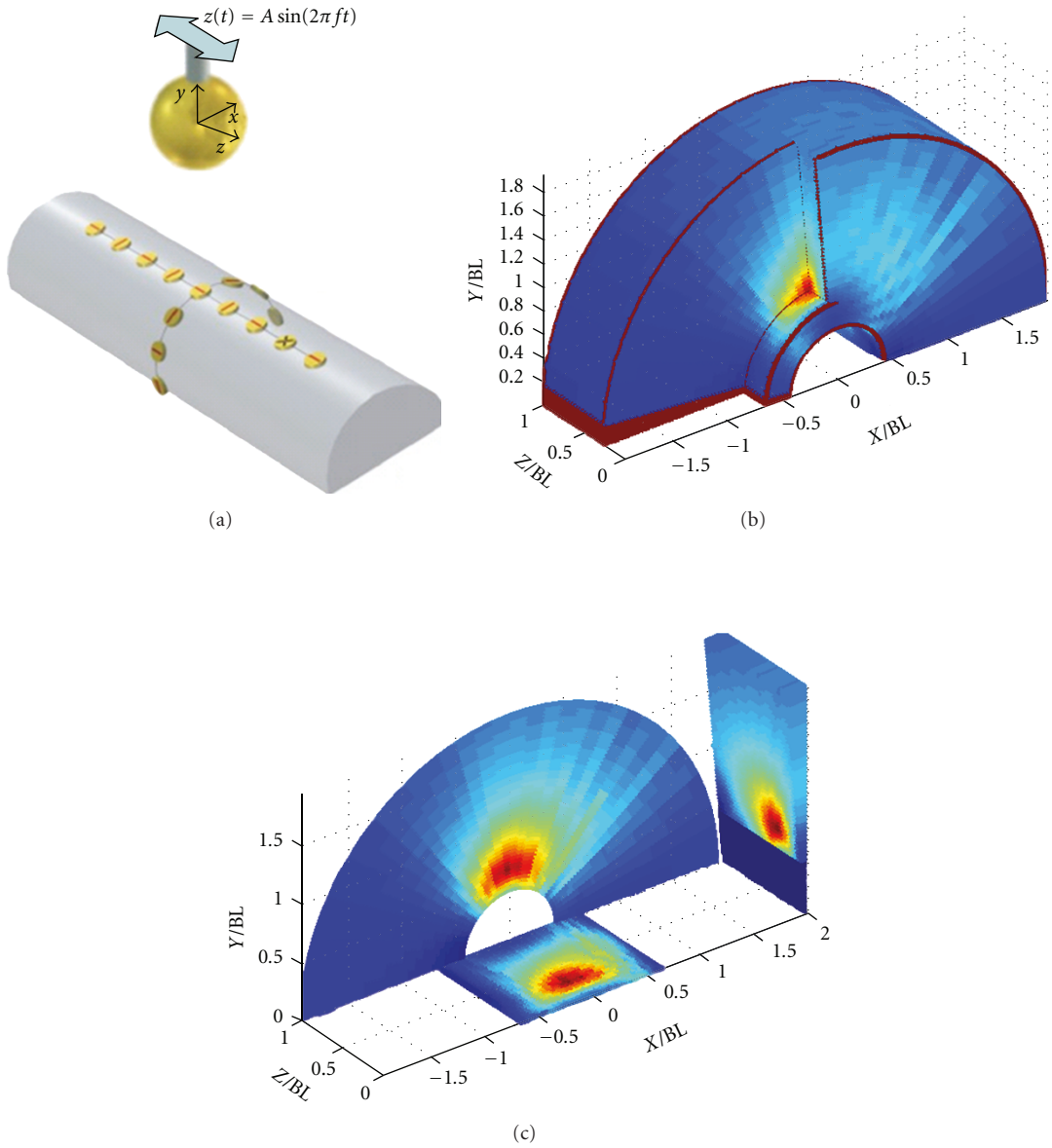

FIGURE 4: A 3D energy-like image of a dipole source at the central position and vibration along the cylinder. (a) A model of the sensor array with a dipole on the top of the central sensor. (b) A 3D image mapping the location of the dipole in space. (c) Projections of the result in (a) by sliding through the estimated dipole location along different surfaces.

of interest in 3D space and for dipole orientations of all different directions. There will thus be five parameters to scan through, including three parameters defining the dipole source position in 3D space and two parameters defining the dipole source vibrating direction. This computation is heavy but can be done once offline.

Executing the beamforming algorithm is straightforward although potentially expensive depending on the size of the array and the scan region. However, this algorithm can be easily implemented as a multithreaded program to enable parallel computing.

For each experimental run, we recorded signals for 10 seconds at a 1 kHz sampling rate. The signals are then bandpass filtered at a central frequency of 45 Hz, which is the vibrating frequency of the dipole source. This step is not necessary although it increases the SNR somewhat; wideband and multiple sources at different frequencies can be imaged without this step.

Figure 4 shows a 3D energy-distribution image demonstrating the localization of a dipole source in front of the center point of the half-cylinder surface at a range of 0.5 BL. There is a well-defined high-energy spot corresponding to the location of the dipole source. Although we search for the best match of the dipole source in both location and vibrating direction, we only display the location on the 3D map. In this case, the estimated vibration orientation also matches well with that of the dipole source, which vibrates along the cylinder's main axis.

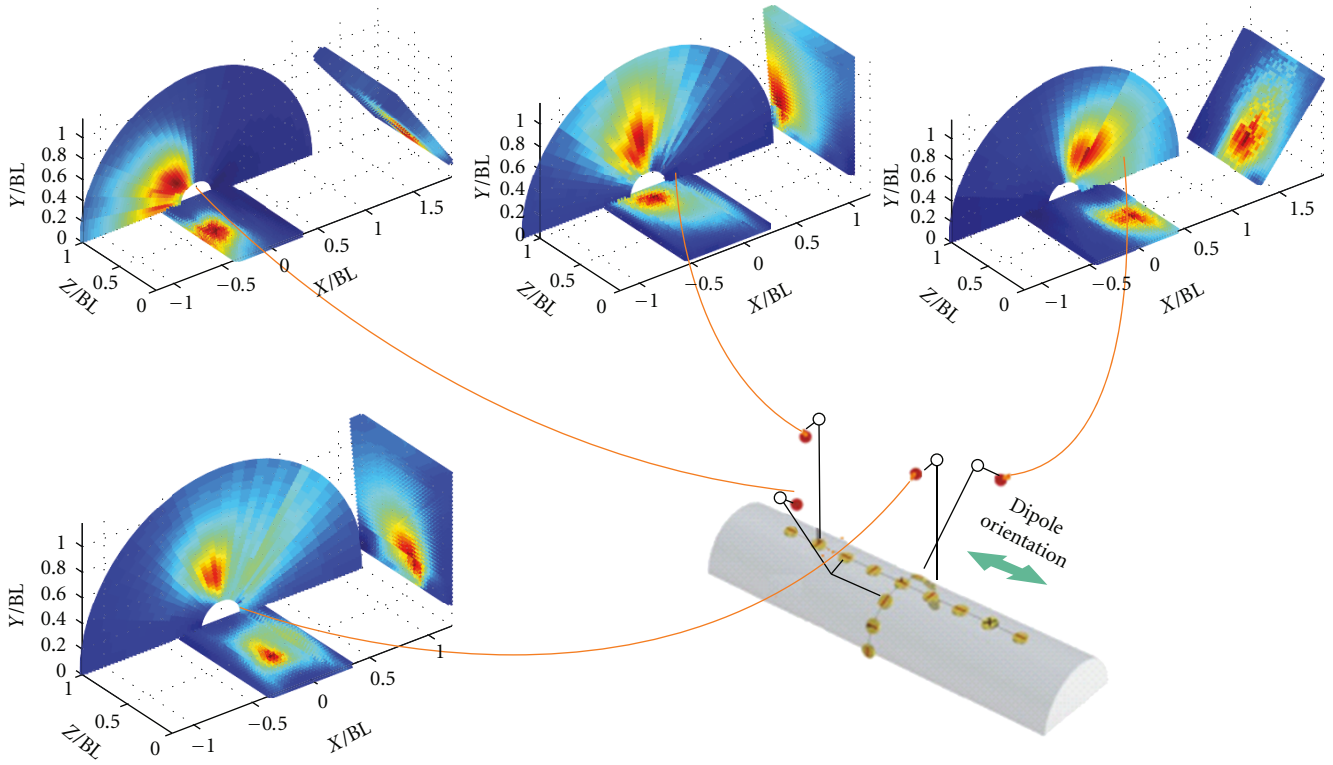

Figure 5: More results of dipole imaging for different locations showing by cutting through the center of the 3D images along the cylinder, across the cylinder, and along the curved surface of the cylinder. The actual dipole locations are represented by black open circles while the estimated locations are indicated by solid circles.

Figure 5 presents the localization results for various positions of the dipole source. The circles represent the actual locations of the dipole source while the red dots represent the estimated ones. In order to have a good view of a 3D image, we slice the 3D image through the peak in three directions, that is, along the cylinder, across the cylinder, and along the curvature of the cylinder. The concentration of the high-energy spots differs for each location of the dipole source, but this is theoretically expected as will be shown in the Cramer-Rao bound analysis in the next section.

5.4. Crayfish Imaging. To further explore the performance of the artificial lateral line in a real-world environment and with real-world signals which are not exactly from dipole sources, we selected a tail-flicking crayfish as a hydrodynamic stimulus. The moving tail of the crayfish was brought near to the cylinder, close to the central sensor (Figure 6(a)). The signal recorded from the central sensor shows a pulsed pattern rather than the sinusoidal patterns generated by the dipole source (Figure 6(b)). However, still using the previous ideal template generated from the dipole source flow model, we applied the beamforming algorithm unaltered to the crayfish data and still achieved sharp localization results as shown in Figure 6(c). This confirms that the proposed method can robustly handle a real-world signal source even just using a simple dipole signal model in the beamforming algorithm.

6. Cramer-Rao Bound

As mentioned in Section 2, the configuration of the lateral line was designed based on knowledge of the fundamental performance limits of our system. Cramer-Rao Lower Bound (CRLB) provides an upper bound on the smallest average estimation error the system could possibly achieve, so we derive the CLRB for a lateral-line array and use it both to optimize the array design and to understand the fundamental performance limits of any lateral-line system.

Consider the model for a signal seen by sensor n in the lateral line as

$$c_n = f_n\left(\vec{d}\right) + w_n, \tag{16}$$

where w_n is additive white Gaussian noise with distribution $\mathcal{N}(0, \sigma_N^2)$, and $f_n(\vec{d})$ is the expected reading at sensor n produced by a dipole at location $\vec{d}$. In our case, $f_n(\vec{d})$ can be computed by (4) and $\vec{d} = (x_d, y_d, z_d)$, the spatial coodinates of the dipole source. Then the CRLB theorem in [20] states that the variance matrix in estimating position vector $\vec{d}$ is limited by

$$\mathrm{Var}\left[\vec{d}\right] \geq [\mathbf{F}]^{-1}, \tag{17}$$

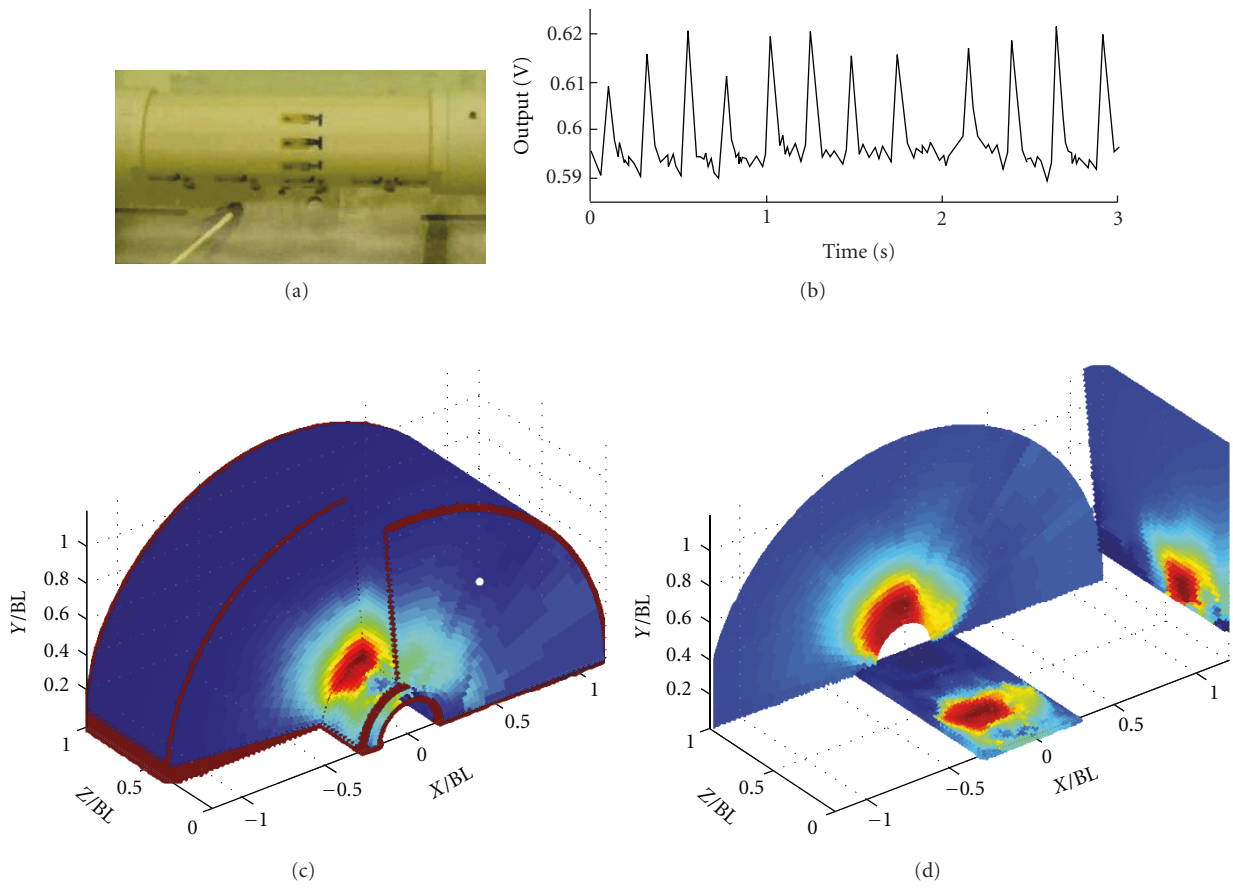

FIGURE 6: Crayfish imaging: (a) An image of a real crayfish flicking its tail near the center of the cylinder. (b) A sample of the tail-flicking signal waveform detected by one sensor in the array. (c) 3D energy image showing the relative level of dynamic flow activities caused by the crayfish (d) Three projections of the 3D image on different surfaces.

where **F** is the Fisher Information Matrix, which can be derived as

$$\mathbf{F} = \frac{1}{\sigma_N^2} \times \begin{bmatrix} \sum_{n=1}^{N} \left(\frac{\partial f_n(x_d, y_d, z_d)}{\partial x_d} \right)^2 & \sum_{n=1}^{N} \frac{\partial f_n(x_d, y_d, z_d)}{\partial x_d} \frac{\partial f_n(x_d, y_d, z_d)}{\partial y_d} & \sum_{n=1}^{N} \frac{\partial f_n(x_d, y_d, z_d)}{\partial x_d} \frac{\partial f_n(x_d, y_d, z_d)}{\partial z_d} \\ \sum_{n=1}^{N} \frac{\partial f_n(x_d, y_d, z_d)}{\partial x_d} \frac{\partial f_n(x_d, y_d, z_d)}{\partial y_d} & \sum_{n=1}^{N} \left(\frac{\partial f_n(x_d, y_d, z_d)}{\partial y_d} \right)^2 & \sum_{n=1}^{N} \frac{\partial f_n(x_d, y_d, z_d)}{\partial y_d} \frac{\partial f_n(x_d, y_d, z_d)}{\partial z_d} \\ \sum_{n=1}^{N} \frac{\partial f_n(x_d, y_d, z_d)}{\partial x_d} \frac{\partial f_n(x_d, y_d, z_d)}{\partial z_d} & \sum_{n=1}^{N} \frac{\partial f_n(x_d, y_d, z_d)}{\partial y_d} \frac{\partial f_n(x_d, y_d, z_d)}{\partial z_d} & \sum_{n=1}^{N} \left(\frac{\partial f_n(x_d, y_d, z_d)}{\partial z_d} \right)^2 \end{bmatrix}. \quad (18)$$

Applying the results above, we computed the CRLB for our system with 14 sensors ($N = 14$), as one sensor was broken during installation. Figure 7 illustrates the CRLB ellipses after projecting onto three planes. The size of each ellipse indicates the performance limit at the corresponding point. The smaller size an ellipse has, the better estimation performance the system could achieve. The slight asymmetry of these uncertainty ellipses is due to a broken sensor at the second position on the right side of the array. From the graphs, we can conclude that the system performs better

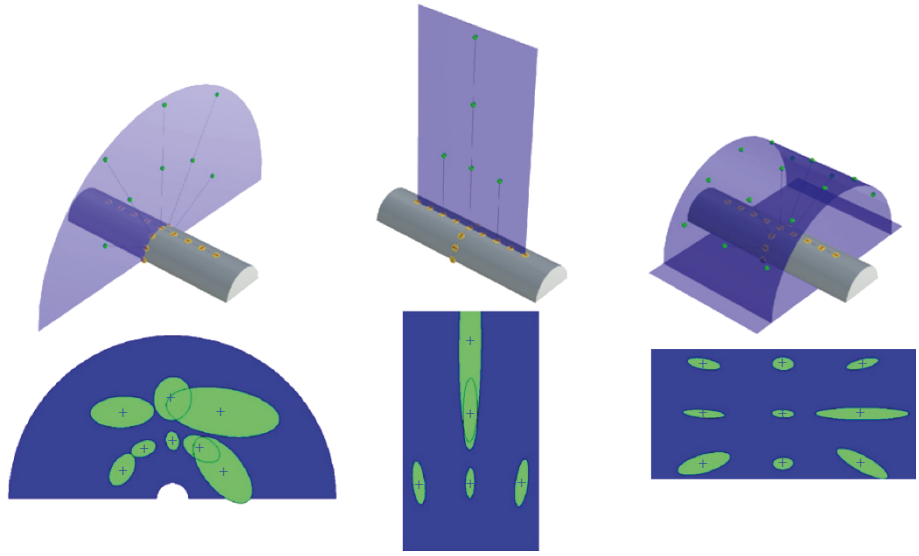

Figure 7: Ellipses display Cramer Rao bounds for different dipole locations by projecting on three planes.

at points in front of the center of the cylinder. As the dipole source moves to the end or the edge of the array, the performance is degraded. Also, the system seems to perform well within the range of one body length of the array. Beyond that one-body-length range, the performance decays very quickly. Thus a lateral-line sense is inherently a short-range, near-field sense.

The CRLB can help to evaluate the performance limit of the system before actually installing sensors on the platform. It can be used as a guide to design a complex sensor array with many sensors.

7. Conclusion

Our results demonstrate the ability of an artificial lateral line system to imitate the sophisticated near-field sensing capability of fish. By showing a complete development from building the MEMS hair-cell sensors, assembling an artificial lateral line, providing signal processing framework and self-calibration algorithms, and deriving the theoretical performance limit, we have confirmed the opportunity of a new application class for near-field sensing in autonomous vehicles and machines. The Cramer-Rao bound confirms mathematically the biological observation that the lateral line imaging capability is confined to the near field. While the method was derived mainly from an idealized dipole model of the signal source, our system shows a good performance and robustness in detecting the tail-flicking signals from a crayfish. This promises a possibility of applying this work on more complicated natural signals.

Acknowledgments

The authors would like to thank their collaborators on the DARPA BioSENSE project. This work was funded by the DARPA BioSENSE project through the AFOSR (Program: FA9550-05-1-0459).

References

[1] S. Dijkgraaf, "The functioning and significance of the lateral-line organs," *Biological Reviews of the Cambridge Philosophical Society*, vol. 38, pp. 51–105, 1963.

[2] S. Coombs and R. A. Conley, "Dipole source localization by mottled sculpin. I. Approach strategies," *Journal of Comparative Physiology A*, vol. 180, no. 4, pp. 387–399, 1997.

[3] S. Coombs and R. A. Conley, "Dipole source localization by the mottled sculpin II. The role of lateral line excitation patterns," *Journal of Comparative Physiology A*, vol. 180, no. 4, pp. 401–415, 1997.

[4] R. A. Conley and S. Coombs, "Dipole source localization by mottled sculpin. III. Orientation after site-specific, unilateral denervation of the lateral line system," *Journal of Comparative Physiology A*, vol. 183, no. 3, pp. 335–344, 1998.

[5] T. J. Pitcher, B. L. Partridge, and C. S. Wardle, "A blind fish can school," *Science*, vol. 194, no. 4268, pp. 963–965, 1976.

[6] J. Chen and C. Liu, "Development of polymer-based artificial haircell using surface micromachining and 3D assembly," in *Proceedings of the 12th International Conference on Solid-State Sensors, Actuators and Microsystems (TRANSDUCERS '03)*, vol. 2, 2003.

[7] C. Liu, "Micromachined biomimetic artificial haircell sensors," *Bioinspiration and Biomimetics*, vol. 2, no. 4, pp. S162–S169, 2007.

[8] B. Ćurčić-Blake and S. M. Van Netten, "Source location encoding in the fish lateral line canal," *Journal of Experimental Biology*, vol. 209, no. 8, pp. 1548–1559, 2006.

[9] Y. Yang, J. Chen, J. Engel et al., "Distant touch hydrodynamic imaging with an artificial lateral line," *Proceedings of the National Academy of Sciences of the United States of America*, vol. 103, no. 50, pp. 18891–18895, 2006.

[10] N. Nguyen, D. Jones, S. Pandya et al., "Biomimetic flow imaging with an artificial fish lateral line," in *Proceedings of the 1st International Conference on Bio-Inspired Systems and Signal Processing (BIOSIGNALS '08)*, pp. 269–276, January 2008.

[11] Y. Yang, N. Nguyen, N. Chen et al., "Artificial lateral line with biomimetic neuromasts to emulate fish sensing," *Bioinspiration and Biomimetics*, vol. 5, no. 1, Article ID 016001, 2010.

[12] Y. Yang, N. Chen, C. Tucker, J. Engel, S. Pandya, and C. Liu, "From artificial hair cell sensor to artificial lateral line system: development and application," in *Proceedings of the 20th IEEE International Conference on Micro Electro Mechanical Systems (MEMS '07)*, pp. 577–580, January 2007.

[13] N. Chen, C. Tucker, J. M. Engel, Y. Yang, S. Pandya, and C. Liu, "Design and characterization of artificial haircell sensor for flow sensing with ultrahigh velocity and angular sensitivity," *Journal of Microelectromechanical Systems*, vol. 16, no. 5, pp. 999–1014, 2007.

[14] A. Schmitz, H. Bleckmann, and J. Mogdans, "Organization of the superficial neuromast system in goldfish, Carassius auratus," *Journal of Morphology*, vol. 269, no. 6, pp. 751–761, 2008.

[15] S. Coombs, "Nearfield detection of dipole sources by the goldfish (Carassius auratus) and the mottled sculpin (Cottus bairdi)," *Journal of Experimental Biology*, vol. 190, pp. 109–129, 1994.

[16] S. Coombs, "Dipole 3d user guide," Tech. Rep., 2003.

[17] S. Pandya, Y. Yang, D. L. Jones, J. Engel, and C. Liu, "Multisensor processing algorithms for underwater dipole localization and tracking using MEMS artificial lateral-line sensors," *EURASIP Journal on Applied Signal Processing*, vol. 2006, Article ID 76593, pp. 1–8, 2006.

[18] D. Johnson and D. Dudgeon, *Array Signal Processing: Concepts and Techniques*, Prentice-Hall, Upper Saddle River, NJ, USA, 1993.

[19] G. Golub and V. Pereyra, "The differentiation of pseudo-inverses and nonlinear least squares problems whose variables separate," *SIAM Journal on Numerical Analysis*, vol. 10, no. 2, pp. 413–432, 1973.

[20] H. Poor, *An Introduction to Signal Detection and Estimation*, Springer, Berlin, Germany, 1994.